Structural and Thermodynamic Investigation of the Perovskite $Ba_2NaMoO_{5.5}$

Kauric, Guilhem; Epifano, Enrica; Martin, Philippe M.; Van Eijck, Lambert; Bouëxière, Daniel; Clavier, Nicolas; Guéneau, Christine; Smith, Anna L.

DOI
10.1021/acs.inorgchem.0c00210

Publication date
2020

Document Version
Final published version

Published in
Inorganic Chemistry

Inorganic Chemistry

pubs.acs.org/IC

Article

Structural and Thermodynamic Investigation of the Perovskite $Ba_2NaMoO_{5.5}$

Guilhem Kauric, Enrica Epifano, Philippe M. Martin, Lambert van Eijck, Daniel Bouëxière, Nicolas Clavier, Christine Guéneau,* and Anna L. Smith*

Cite This: *Inorg. Chem.* 2020, 59, 6120−6130

Read Online

ACCESS | Metrics & More | Article Recommendations | Supporting Information

ABSTRACT: Neutron diffraction, X-ray absorption spectroscopy (XAS), and Raman spectroscopy measurements of the quaternary perovskite phase $Ba_2NaMoO_{5.5}$ have been performed in this work. The cubic crystal structure in space group $Fm\bar{3}m$ has been refined using the Rietveld method. X-ray absorption near-edge structure spectroscopy (XANES) measurements at the Mo K-edge have confirmed the hexavalent state of molybdenum. The local structure of the molybdenum octahedra has been studied in detail using extended X-ray absorption fine structure (EXAFS) spectroscopy. The Mo−O and Mo−Ba distances have been compared to the neutron diffraction data with good agreement. The coefficient of thermal expansion measured in the temperature range of 303−923 K, using high temperature X-ray diffraction (HT-XRD) (α_V = 55.8 × 10^{-6} K), has been determined to be ∼2 times higher than that of the barium molybdates $BaMoO_3$ and $BaMoO_4$. Moreover, no phase transition nor melting have been observed, neither by HT-XRD nor Raman spectroscopy nor differential scanning calorimetry, up to 1473 K. Furthermore, the standard enthalpy of formation ($\Delta_f H_m^\circ$) for $Ba_2NaMoO_{5.5}$(cr) has been determined to be −(2524.75 ± 4.15) kJ mol^{-1} at 298.15 K, using solution calorimetry. Finally, the margin for safe operation of sodium-cooled fast reactors (SFRs) has been assessed by calculating the threshold oxygen potential needed, in liquid sodium, to form the quaternary compound, following an interaction between irradiated mixed oxide $(U,Pu)O_2$ fuel and sodium coolant.

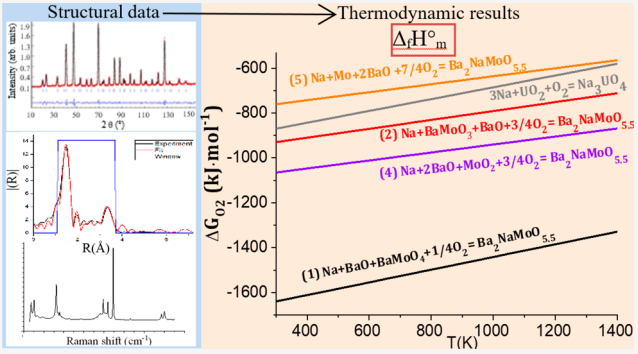

1. INTRODUCTION

Sodium-cooled fast reactors (SFRs) are, in terms of performance and safety, among the most advanced designs for the next generation (Generation IV) of nuclear reactors.[1] SFRs use metallic sodium as a coolant and heat-transfer medium, allowing high power density with low coolant volume fraction.[1] $(U,Pu)O_{2-x}$ is currently the reference fuel for this type of reactor, with a plutonium content of ∼20−30 wt %.

During operation and irradiation, fission products such as molybdenum and barium are generated with a high fission yield in the ceramic fuel matrix. Past studies have shown that these elements form oxide precipitates, more specifically $BaMoO_3$ dissolved in the gray phase $(Ba,Sr,Cs)(Zr,U,Pu,Mo,RE)O_3$, (RE = rare earths) and/or $BaMoO_4$ depending on temperature, oxygen potential conditions, and burnup.[2−7] In particular, the recent PHEBUS FPT2 test within the PHEBUS FP Program (which is a study of the degradation of the core and the fission products release in case of an accident) has shown a clear association of Mo and Ba in oxide precipitates at grain boundaries in fuel test sections.[7] In case of a severe accident (an accident where the reactor fuel is damaged with possible melting of the reactor core),[8] the fission product compounds within the fuel pellet would interact with sodium on a large temperature scale (from 900 K to >3000 K). To assess the safety of the reactor, the possible reaction products between sodium and barium−molybdenum fission product phases must be investigated. Structural and thermodynamic investigation of the Ba−Mo−Na-O system is a first step, and it can serve as input for the development of comprehensive thermodynamic models of the multicomponent system Ba-Cs-Na-Mo-Sr-Zr-U-Pu-RE-O,[9−11] using the CALPHAD methodology.[12]

The quaternary compound $Ba_2NaMoO_{5.5}$ was reported by Sabatier et al.,[13] who synthesized this compound while attempting to form a layered perovskite. This compound has also been studied for its high oxide-ion conductivity at relatively low temperatures (∼850 K) by Thangadurai et al.,[14] which is a property particularly interesting to develop commercially viable solid oxide fuel cells (SOFCS). Among the

Received: January 20, 2020
Published: April 20, 2020

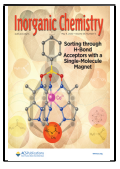

studied oxygen-deficient double perovskites $Ba_2BB'O_{5.5}$ (B = Li, Na; B′ = Mo, W, Te), $Ba_2NaMoO_{5.5}$ has shown the highest conductivity. However, thermophysical properties and chemical behavior of the aforementioned compound at high temperatures have not been determined to this date. These data are key for the prediction of the behavior of the irradiated fuel and the phase formation in case of an accident in the SFR, as Ba-Mo-O phases are found in the irradiated fuel and are very likely to react with the sodium coolant.

This work reports neutron diffraction and X-ray absorption spectroscopy (XAS) measurements on $Ba_2NaMoO_{5.5}$ at room temperature, which have allowed to assess and refine the atomic oxygen positions and vacancies in the structure precisely. Moreover, the thermal expansion and thermal stability of the compounds were studied using high-temperature X-ray diffraction (HT-XRD), high-temperature Raman spectroscopy, and differential scanning calorimetry (DSC). The standard enthalpy of formation of $Ba_2NaMoO_{5.5}$ at 298.15 K was measured via solution calorimetry. Using these newly determined data, the likelihood of formation of this quaternary compound in the irradiated fuel by reaction between the sodium coolant and $\{BaMoO_4 + BaO\}$ or $\{BaMoO_3 + BaO\}$ fission product phases was finally assessed.

2. EXPERIMENTAL SECTION

2.1. Synthesis Method. $Ba_2NaMoO_{5.5}$ was synthesized by reaction between barium molybdate ($BaMoO_4$) and stoichiometric amounts of barium carbonate ($BaCO_3$) (Fluka, >99%) and anhydrous sodium carbonate Na_2CO_3 (Sigma−Aldrich, >99.5%). The stoichiometric mixture was heated under oxygen flow at 973 K for 60 h with intermediate regrinding steps. Samples were analyzed by X-ray and neutron diffraction at room temperature.

The starting reagent $BaMoO_4$ was synthesized by grinding barium carbonate $BaCO_3$ (Fluka, >99%) and molybdenum trioxide MoO_3 (Alfa Aesar, >99.5%) together in stoichiometric ratio and heating under dry oxygen at 1073 K for 45 h with intermediate regrinding steps. Samples were analyzed by X-ray and neutron diffraction at room temperature (see Figure S1 in the Supporting Information).

$Na_2Mo_2O_7$ was synthesized for solution calorimetry measurement purposes by heating a stoichiometric mixture of anhydrous Na_2CO_3 (Sigma−Aldrich, 99.5%) and Na_2MoO_4 (Sigma−Aldrich, 99.5%) under dry oxygen at 773 K for 60 h with intermediary regrinding. The sample then was checked by XRD and DSC measurements (see Figures S2 and S3 in the Supporting Information).

In every analysis, no secondary phase was observed. Therefore, the purity of every compound is expected to be better than 99.5%.

2.2. Neutron Diffraction. Neutron data were collected at the Hoger Onderwijs Reactor at TU Delft[15] at the PEARL beamline. The sample was encapsulated under an argon atmosphere in a cylindrical vanadium can (50 mm high, 6 mm inner diameter) closed with a Viton O-ring. The data were collected at room temperature, at a fixed wavelength λ = 1.667 Å for 6 h and λ = 1.33 Å for 12 h over a range of $11° \leq 2\theta \leq 158°$. The Rietveld method implemented in the Fullprof2k suite[16] was used for the structural analysis.

2.3. Powder X-ray Diffraction. X-ray diffraction (XRD) data at room temperature were collected using a PANalytical X'Pert PRO X-ray diffractometer mounted in the Bragg−Brentano configuration with a Cu anode (Cu Kα_1, λ = 1.541 Å, Cu Kα_2, λ = 1.544 Å) (0.4 mm × 12 mm line focus, 45 kV, 40 mA) and a real-time multi strip (RTMS) detector (X'Celerator). Diffraction patterns were obtained by step scanning in step sizes of 0.008° (2θ) in the angle range of $10° \leq 2\theta \leq 120°$ with an integration time of ∼8 h. The Rietveld method implemented in the Fullprof2k suite[16] was used for the structural analysis.

2.4. High-Temperature X-ray Diffraction (HT-XRD). The thermal expansion of $Ba_2NaMoO_{5.5}$ was investigated by HT-XRD using a Bruker Model D8 X-ray diffractometer mounted with a curved Ge monochromator (111), a copper ceramic X-ray tube (40 kV, 40 mA), a Linx Eye position-sensitive detector, and equipped with an Anton Paar HTK 2000 chamber. Measurements were conducted in a 600 mbar helium atmosphere from room temperature up to 1223 K, with 100 K heating steps. The temperature, measured with a thermocouple, was previously calibrated using the thermal expansion data of MgO.[17] The uncertainty on the temperature is estimated to be 20 K at 1223 K.

2.5. X-ray Absorption Spectroscopy (XAS). XAS data were collected at the BM26A-DUBBLE beamline of the European Synchrotron Radiation Facility (ESRF) in Grenoble (France).[18] For the XAS measurements, ∼20 mg of powdered samples were mixed with boron nitride (BN), pressed into pellets and encapsulated in Kapton foils. The aforementioned operations were performed inside an argon-filled glovebox, where oxygen and water levels were kept below 1 ppm. The storage ring operating conditions were 6.0 GeV and 170−200 mA. A double crystal monochromator mounted with a Si(111) crystal coupled to collimating and focusing Pt coated mirrors was used. Rejection of higher harmonics was achieved by three Si mirrors at an angle of 2 mrad, relative to the incident beam.

XANES and EXAFS spectra were collected at room temperature, in transmission mode at the Mo K-edge. A step size of 1 eV was used in the edge region. The energy of the edge absorption threshold position (E_0) was taken at the inflection point of the spectrum by using the first node of the second derivative. The position of the prepeak in the edge was selected from the first node of the first derivative. Several acquisitions were performed on the same sample and averaged to improve the signal-to-noise ratio. Before averaging the scans, each spectrum was aligned using the XANES spectrum of a metallic molybdenum reference foil measured before and after the sample under investigation. The ATHENA software[19] was used to normalize the spectra and extract the EXAFS signal from the raw data.

The EXAFS data were collected in this work, up to 15 $Å^{-1}$, and were Fourier-transformed using the Hanning window over the k-range of 3.5−13.5 $Å^{-1}$ (dk = 1). Curve fitting was performed based on the standard EXAFS equation using the ARTEMIS software[19] in k-, k^2-, and k^3-space. Phases and amplitudes for the interatomic scattering paths were calculated with the ab initio code FEFF8.40.[20] The shift in the threshold energy (ΔE_0) was varied as a global parameter. The amplitude factor S_0^2 was fixed for all paths to 0.9. The coordination numbers, Debye−Waller factors, and interatomic distances parameters, i.e., N, σ^2 and R, respectively, were allowed to vary for each shell.

2.6. High-Temperature Raman Spectroscopy. High-temperature Raman spectra were recorded using a Horiba Jobin-Yvon Aramis spectrometer equipped with a Linkam TS-1500 heating device. The $Ba_2NaMoO_{5.5}$ sample was placed in a platinum crucible and inserted in the furnace. A rate of 10 K min^{-1} was applied upon heating, and 5 min of stabilization time was maintained at each temperature plateau before acquisition of the spectra. The 632.8 nm line of a He−Ne laser was used as the excitation wavelength and focused by means of an Olympus BX41 (magnification factor of 50×), thus delivering ∼10 mW at the sample surface. Slits and a confocal hole were set to result in a resolution of 1 cm^{-1}. For each spectrum, an acquisition time of 4 s was considered with an average of four scans. Before analysis, the apparatus was calibrated with a silicon wafer, using the first-order Si line at 520.7 cm^{-1}. Band component analysis of the different spectra was performed with the Jandel Peakfit software, using pseudo-Voigt functions with the minimum number of components. Correlation coefficients of >0.997 were systematically obtained.

2.7. Differential Scanning Calorimetry. Three-dimensional (3D)-heat-flow DSC measurements were performed from 303 K up to 953 K for $Na_2Mo_2O_7$ and up to 1473 K for $Ba_2NaMoO_{5.5}$, using a Setaram Multi HTC module of the 96 Line calorimeter. The sample (80.7 mg for $Na_2Mo_2O_7$ and 80.3 mg for $Ba_2NaMoO_{5.5}$) was placed in an alumina liner and encapsulated for the calorimetric measurements inside a stainless steel crucible that was closed with a screwed bolt to avoid vaporization at high temperatures.[21] The measurement was done as follows: four successive heating cycles with a heating rate of 5 K min^{-1}, and cooling rates of 5, 8, 10, and 12 K min^{-1}. The temperature was monitored by a series of interconnected S-types

https://dx.doi.org/10.1021/acs.inorgchem.0c00210
Inorg. Chem. 2020, 59, 6120−6130

thermocouples, and corrected on the heating ramp using a temperature calibration equation obtained from the measurement of standard materials (In, Pb, Sn, Zn, Al, Ag, Au) of well-known melting temperatures. The transition temperatures were derived on the heating ramp as the onset temperatures, using tangential analysis of the recorded heat flow.

2.8. Solution Calorimetry. The enthalpies of dissolution of $Ba_2NaMoO_{5.5}$, BaO, and $Na_2Mo_2O_7$ in 2 M nitric acid solution were measured using a TA Instruments Precision Solution calorimeter (semiadiabatic or isoperibolic calorimeter) and a TAM IV thermostat. The calorimetric unit consists of a reaction vessel and stirrer holding a glass ampule. The experiments were performed in a thin-walled 100 mL Pyrex-glass reaction vessel equipped with a thermistor for measuring the temperature rise, and a heater for calibration during the measurement and equilibration of the initial baseline in the optimal operating range of the calorimeter before starting the experiment. The samples under study (BaO, $Na_2Mo_2O_7$, $Ba_2NaMoO_{5.5}$) were placed inside a 1 mL glass ampule, which was sealed with bee wax. The latter operation was performed in the dry atmosphere of an argon-filled glovebox, because of the sensitivity of the samples to air and moisture. The solid samples were dissolved into a solution of 2 M HNO_3 by breaking the bottom of the glass ampule on the sapphire breaking tip mounted at the bottom of the reaction vessel. The heat produced when breaking the ampule is exothermic, with a value below 10 mJ, and can thus be neglected (measured values are more than 1 J $\gg$ 10 mJ). The temperature during the measurements was maintained in the oil bath with an accuracy of $\pm 1.10^{-4}$ K. Electrical calibrations were performed immediately before and after each enthalpy of reaction measurement to determine the equivalent energy of the system.

The accuracy of the measurements was verified by measuring the enthalpy of dissolution of potassium chloride (KCl, Sigma–Aldrich, 99.7%) in distilled water. The experimentally determined dissolution enthalpy of $KCl_{(cr)}$ into $1000H_2O$ (molality m = 0.05551 mol kg^{-1}), i.e., $\Delta_{diss}H^{\circ}_m(1000H_2O, 298.15\ K)$ = (17.467 ± 0.011) kJ mol^{-1} corresponds to $\Delta_{diss}H^{\circ}_m(500H_2O, 298.15\ K)$ = (17.517 ± 0.011) kJ mol^{-1} after correction to m = 0.111 mol kg^{-1}. The correction mentioned here was performed as recommended by the NBS:[22] the measured dissolution enthalpy was corrected to the molality of the certified enthalpy value m = 0.111 mol kg^{-1}, using the relationship $\Delta H^{\circ}(500H_2O, 298.15\ K) = \Delta H(nH_2O, 298.15\ K) - \{\Phi L(nH_2O) - \Phi L(500H_2O)\}$. $\Delta H(nH_2O, 298.15\ K)$ is the measured dissolution enthalpy corrected to the reference temperature, and the term $\{\Phi L(nH_2O) - \Phi L(500H_2O)\}$, derived from Parker's tabulation[23] and listed by NBS,[22] corrects the molality to the certified value. The uncertainty on the correction was estimated not to exceed 5 J mol^{-1}.[22]

The measured value corresponds to an enthalpy at infinite dilution of $\Delta_{diss}H^{\circ}_m(\infty H_2O, 298.15\ K)$ = (17.174 ± 0.011) kJ mol^{-1}, in good agreement with the NBS data,[22,24] i.e., $\Delta_{diss}H^{\circ}_m(\infty H_2O, 298.15\ K)$ = (17.241 ± 0.018) kJ mol^{-1}, and that in ref 25, i.e., $\Delta_{diss}H^{\circ}_m(\infty H_2O, 298.15\ K)$ = 17.22 kJ mol^{-1}.

3. RESULTS AND DISCUSSION

3.1. Refinement of the $Ba_2NaMoO_{5.5}$ Structure Using X-ray and Neutron Diffraction. $Ba_2NaMoO_{5.5}$ crystallizes at room temperature with a cubic perovskite structure in space group $Fm\bar{3}m$ (No. 225).[13] The collected X-ray and neutron diffraction patterns are reported in Figures 1 and 2. The refined cell parameter obtained from the Rietveld refinement of the XRD data, a = 8.3156(4) Å, is consistent with the value reported by Thangarudai et al.[14] (a = 8.319(3) Å). The neutron diffraction data (a = 8.305(1) Å at λ = 1.667 Å and a = 8.303(1) Å at λ = 1.33 Å) are consistent with the XRD results, as seen in Table 1. The atomic positions obtained after the Rietveld refinement of the neutron diffraction data are reported in Table 2 (data at λ = 1.667 Å) and Table S1 in the Supporting Information (data at λ = 1.33 Å). The results obtained from the two neutron diffraction measurements are similar. The measurement at λ = 1.33 Å gives extra information

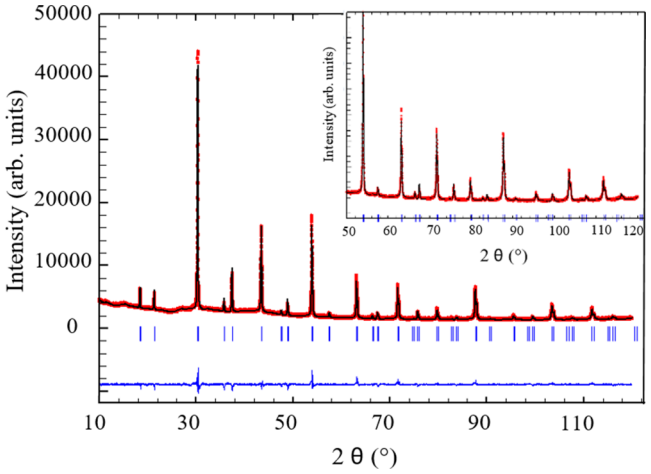

Figure 1. Comparison between the calculated (Y_{calc}, in black) and observed (Y_{obs}, in red) XRD patterns of $Ba_2NaMoO_{5.5}$. $Y_{obs} - Y_{calc}$ (in blue) is the difference between the observed and calculated intensities. The angular positions of Bragg reflections are shown in blue. The measurement has been performed at λ = Cu Kα with Cu Kα_1, λ = 1.541 Å, Cu Kα_2, λ = 1.544 Å.

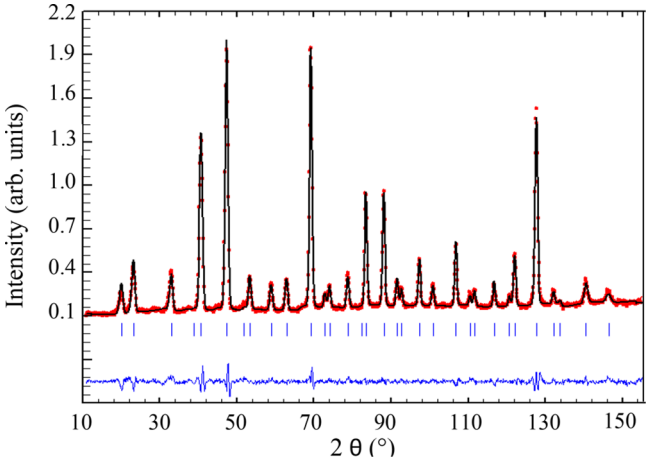

Figure 2. Comparison between the calculated (Y_{calc}, in black) and observed (Y_{obs} in red) neutron diffraction patterns of $Ba_2NaMoO_{5.5}$. $Y_{obs} - Y_{calc}$ (in blue) is the difference between the observed and calculated intensities. The angular positions of Bragg reflections are shown in blue. The measurement has been performed at λ = 1.667 Å.

on peaks at high angles (Figure S4 in the Supporting Information). However, the resolution of the peaks is decreasing.[26]

$Ba_2NaMoO_{5.5}$ shows a perovskite-type structure with infinite chains of alternating corner-sharing MoO_6 and NaO_6 regular octahedra, along the a-, b-, and c-axes, as shown in Figure 3. These regular octahedra have distances of 2.220(2) Å for Na–O bonds and 1.933(2) Å for Mo–O bonds. Moreover, the presence of oxygen vacancies is assessed by the refined occupancy factor on the 24e site of the oxygen. The refined occupancy, i.e., 0.91(1), yields a chemical composition corresponding to 5.46(6) oxygen atoms per formula unit, which is consistent with the theoretical formula (5.5). Ba atoms are located in the center of a cube formed by the alternating NaO_6/MoO_6 octahedra, as illustrated in Figure 3, in 12 coordination, with Ba–O distances of 2.940(1) Å and Mo–Ba and Na–Ba distances of 3.596(1) Å. The thermal displacement factors B_0 for the Na atom in both refinements of

https://dx.doi.org/10.1021/acs.inorgchem.0c00210
Inorg. Chem. 2020, 59, 6120–6130

Table 1. Profile Parameters of $Ba_2NaMoO_{5.5}$ Obtained with the Different Diffraction Methods[a]

parameter	Value		
	XRD	neutron	
chemical formula	$Ba_2NaMoO_{5.5}$	$Ba_2NaMoO_{5.5}$	
formula weight (g mol^{-1})	481.6	481.6	
temperature (K)	(293 ± 3)	(293 ± 3)	
wavelength, λ (Å)	1.541/1.544	1.667	1.33
crystal system	cubic	cubic	
space group	$Fm\bar{3}m$ (No. 225)	$Fm\bar{3}m$ (No. 225)	
a (Å)	8.3156(4)	8.305(1)	8.303(1)
cell volume, V (Å^3)	575.01(8)	572.9(3)	572.3(2)
Z	4	4	
d-space range (Å)	0.89−8.84	0.78−8.35	0.78−8.35
χ^2	6.59	3.85	2.74
R_p	18.4	10.1	9.77
R_{wp}	13.3	5.14	5.9

[a]Definition of R-factors hereafter: $\chi^2 = \sum_k w_k(y_{ck} - y_{ok})^2/(N-P)$, where N is the number of observations and P the number of parameters used in the refinement, w_k the weights of the observations, y_{ck} the calculated counts, and y_{ok} the observed counts at the k-step. R_p is the profile factor: $R_p^2 = \sum_k (y_{ck} - y_{ok})^2/\sum_k (y_{ok})^2$. R_{wp} is the weighted profile factor: $R_{wp}^2 = \sum_k w_k(y_{ck} - y_{ok})^2/\sum_k (y_{ok})^2$.

neutron diffraction patterns are lower than the other atoms. This could be related to the ordering of this crystallographic site, as observed for the Co site in the La_2CoMnO_6 perovskite compound reported by Kumar and Sathe.[27]

3.2. X-ray Absorption Spectroscopy. *X-ray Absorption Near-Edge Structure Analysis.* The XANES spectrum of $Ba_2NaMoO_{5.5}$, collected at the Mo K-edge, are reported in Figure 4, together with that of Mo^0 metal, $Mo^{IV}O_2$, and α-$Mo^{VI}O_3$ reference materials.

The energy position of the inflection points are listed in Table 3. The E_0 value for $Ba_2NaMoO_{5.5}$ is similar to that of MoO_3, confirming the oxidation state +VI of molybdenum in this material. This result was expected, given that the synthesis reaction consisted in the stoichiometric reaction between hexavalent $BaMoO_4$, $BaCO_3$, and Na_2CO_3 starting materials under oxygen flow. The $BaMoO_4$ starting material was itself prepared from hexavalent MoO_3 and $BaCO_3$ materials. A shift of E_0 to higher energies is also observed with increasing oxidation state, as expected. In addition, the spectrum of α-MoO_3 shows a prepeak at ∼20007.6(5) eV, which is observed as a shoulder, because of the core hole broadening. This prepreak comes from to the hybridization of O(2p) with Mo(4d) and Mo(5p) and thus corresponds to 1s(Mo) → 5p + 4d(Mo) transition.[28−30]

EXAFS Analysis. The Mo K-edge fitted and experimental EXAFS data are reported hereafter (see Figure 5). The path corresponding to the six Na atoms surrounding the Mo were not taken into account for the fitting, because their intensity is too weak.

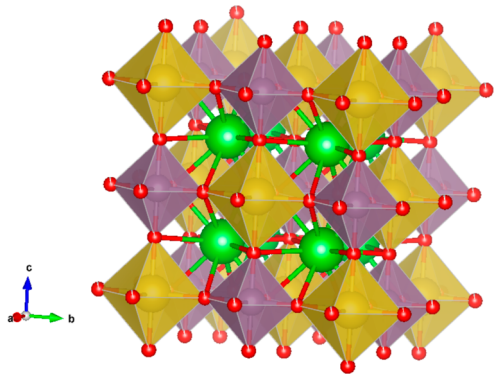

Figure 3. Sketch of the structure of $Ba_2NaMoO_{5.5}$. The octahedrons around the Mo and Na atoms are represented in purple and yellow, respectively. Ba atoms are represented in green, and O atoms are shown in red.

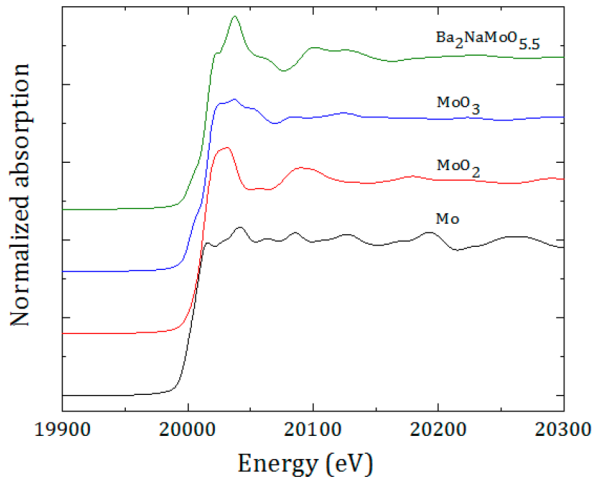

Figure 4. XANES spectra of the $Ba_2NaMoO_{5.5}$ compound obtained at the Mo K-edge and comparison with spectra of Mo^0, $Mo^{IV}O_2$, and $Mo^{VI}O_3$ used as a reference.

Table 3. Energy Position of the Inflection Points for the Reference Materials and $Ba_2NaMoO_{5.5}$

Compound	E_0[a] (eV)
$Ba_2NaMoO_{5.5}$	20015.2
$Mo^{VI}O_3$	20015.7
$Mo^{IV}O_2$	20012.0
Mo^0	20000.0

[a]The standard uncertainties u on the energy position of the inflection points are $u(E_0)$ = 1 eV.

Table 2. Refined Atomic Positions, Isotropic Thermal Displacement Factor (B_0) and Occupancy in the $Ba_2NaMoO_{5.5}$ Compound (Noted as Occ. in the Table) Derived from the Neutron Refinement at λ = 1.667 Å[a]

atom	oxidation state	Wyckoff	x	y	z	B_0(Å^2)	Occ.
Ba	+2	8c	0.25	0.25	0.25	1.34(3)	1
Na	+1	4a	0	0	0	0.80(8)	1
Mo	+6	4b	0.5	0.5	0.5	1.38(5)	1
O	−2	24e	0.2673(2)	0	0	1.98(2)	0.91(1)

[a]Background obtained by linear interpolation between operator-selected points in the pattern with refinable heights.

https://dx.doi.org/10.1021/acs.inorgchem.0c00210
Inorg. Chem. 2020, 59, 6120−6130

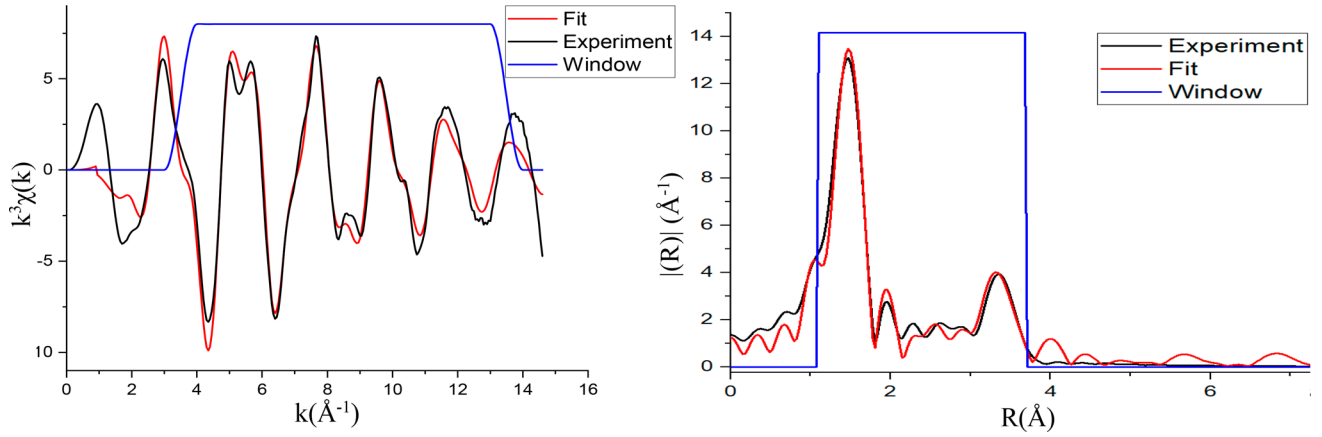

Figure 5. Fitted (red) and experimental (black) $k^3\chi(k)$ spectra and Fourier transform of $Ba_2NaMoO_{5.5}$ obtained at room temperature. (Fourier transform boundaries: 3.5−13.5 $Å^{-1}$, dk = 1 $Å^{-1}$).

The number of O (5.6(2)) and Ba (8) atoms in the first and second coordination shells around Mo determined with EXAFS are consistent with the theoretical formula and the neutron diffraction data (5.46(6)). The Mo−Ba distances obtained by EXAFS and neutron diffraction measurements, reported in Table 4, are in good agreement within uncertainties. As for the O atoms, the Mo−O bond lengths derived by EXAFS are slightly lower than those obtained by neutron diffraction for the first sphere. Based on the amplitude of the Mo−O−Mo−O path in the EXAFS signal calculated by FEFF (35%, compared to 37% for the Mo−Ba path), a multiscattering path[#] (designed hereafter with an asterisk (*)), involving two O atoms of the first coordination shell, was added for the fitting to reproduce the experimental data satisfactorily. However, to minimize the refined parameter during the fitting process, the coordination number of the multiscattering path* was fixed to the value taken for the first coordination shell. The bond length that was finally optimized was determined to be longer than twice the value obtained for the single scattering Mo−O path (i.e., 3.98(2)/2 = 1.99(1) Å, compared to 1.89(1) Å).

Table 4. Bond Lengths (R_E) of $Ba_2NaMoO_{5.5}$ Obtained from EXAFS and Neutron Diffraction Data (R_N)[a]

bond	number of atoms in each shell, N	R_E (Å)	Debye−Waller factor, σ^2	R_N (Å)
Mo−O	5.6(2)	1.89(1)	0.0047(8)	1.933(2)
Mo−Ba	8	3.62(2)	0.014(2)	3.596(1)
Mo−O−Mo−O	5.6(2)	3.98(2)	0.017(2)	3.866(4)

[a]For the EXAFS fitting (ΔE_0 = 3.1, goodness of fit = $\frac{\sum_k(\text{data}_k - \text{fit}_k)^2}{\sum_k(\text{data}_k)^2}$ = 0.017). Standard deviations are given in parentheses.

Such a difference between single and multiple-scattering paths within the BO_6 unit of a ABO_3 perovskite have already been observed in $La_{2-x}Sr_xCu_{1-y}Ru_yO_{4-\delta}$.[26] In such material, the BO_6 octahedra are known to rotate or tilt to adjust for different sizes of A cations[27] which induces a slight loss of linearity (0° angle) of the O(1)−Mo−O(2) section of the multiscattering path*. Such phenomenon would then induce an increase of the associated distance,[28] compared to the strict sum of the two single-scattering Mo−O paths. To check the validity of such hypothesis, the average Mo−O bond distances of single and multiscattering paths* can be easily compared to the 1.933(2) Å given by neutron diffraction measurements. The average Mo−O given by EXAFS is equal to 1.94(2) Å similar to the neutron value. Hence, this is consistent with the hypothesis of a tilting of the octahedra in the structure of $Ba_2NaMoO_{5.5}$.

Finally, possible anharmonicity effects were considered. However, during the fit of the EXAFS data, it was not necessary to introduce any anharmonicity parameter (cumulant term), neither in the O shell nor the Ba shell to reproduce the experimental data. Thus, the oxygen vacancy observed in the oxygen coordination shell does not introduce a non-Gaussian distribution of the Mo−O distances.

3.3. High-Temperature Behavior. The assessment of the thermal expansion behavior of $Ba_2NaMoO_{5.5}$ is key for the safety analysis of an accidental scenario in a SFR to determine the effect on the swelling of the fuel due to the formation of a quaternary compound. The evolution of the cell parameters, as a function of temperature, was determined by Rietveld refinement of the HT-XRD data (see Table S2 in the Supporting Information). No change was observed between the XRD patterns obtained up to the maximum temperature of the measurement (T = 1223 K). Only a shift to lower 2θ values was observed following the expansion of the unit cell. The relative thermal expansion of the unit lattice parameters is reported in Figure 6 between room temperature and T = 1223 K. The mean relative linear thermal expansion coefficient, $\frac{dl}{l_0}$, where $l = (abc)^{1/3}$ and $l_0 = (a_0b_0c_0)^{1/3}$ is the reference length at 303 K, can be expressed as a polynomial function of the temperature T(K) (see eq 1):

$$\frac{dl}{l_0} = -3.69 \times 10^{-3} + 1.0047 \times 10^{-5}T + 6.74121 \times 10^{-9}T^2 \quad (1)$$

The plots of relative expansion, $\frac{l - l_0}{l_0} = f(T)$, for the compounds $Ba_2NaMoO_{5.5}$, $BaMoO_4$,[31] and $BaMoO_3$[32] are shown hereafter (see Figure 6):

The mean relative linear thermal expansion of the quaternary compound is ~2 times higher than that of the two barium molybdates $BaMoO_3$ and $BaMoO_4$, which are thermodynamically stable under certain operating conditions. The average volumetric thermal expansion of $BaMoO_4$ and $BaMoO_3$ are equal to α_V = 26.6 × 10^{-6} K^{-1} and 28.4 × 10^{-6}

https://dx.doi.org/10.1021/acs.inorgchem.0c00210
Inorg. Chem. 2020, 59, 6120−6130

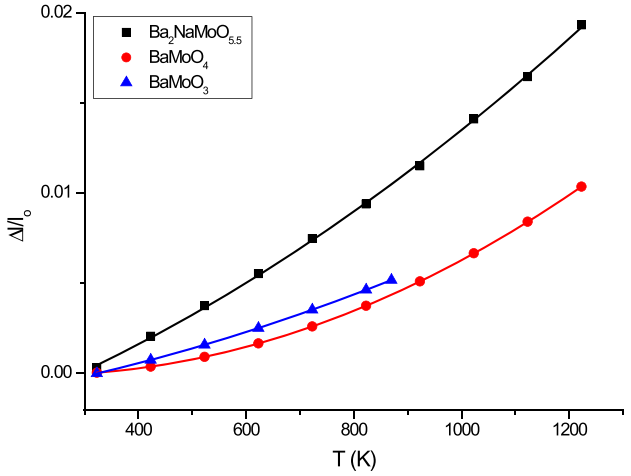

Figure 6. Relative thermal expansion of $Ba_2NaMoO_{5.5}$, compared to $BaMoO_4$[31] and $BaMoO_3$.[32]

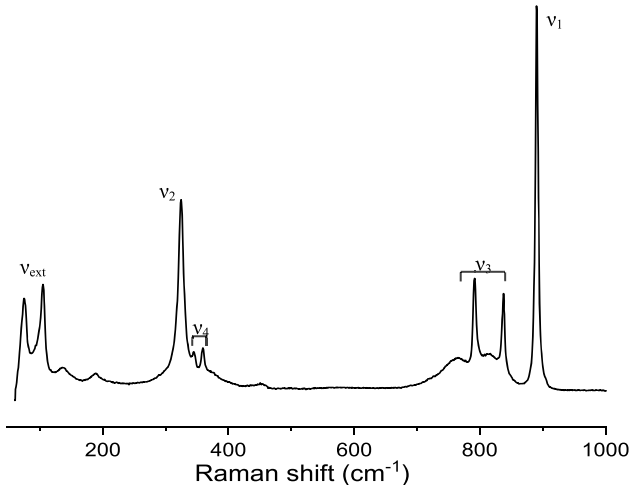

Figure 7. Raman spectrum of $Ba_2NaMoO_{5.5}$ obtained at 298 K.

K^{-1} in the temperature ranges of 298−1273 K and 298−873 K, respectively.[31,32] In comparison to these values, the average volumetric thermal expansion of $Ba_2NaMoO_{5.5}$ is ∼2 times higher: 55.8×10^{-6} K^{-1} in the temperature range of 303−1223 K. This distinct property of the quaternary compound can be related to the local structure properties. In particular, when comparing the structure of $Ba_2NaMoO_{5.5}$ with that of $BaMoO_3$, which is also a cubic perovskite, one can note that the local structural arrangement is similar, but also that the introduction of Na atoms into the three-dimensional (3D) network is responsible for the observed high-temperature behavior. In $BaMoO_3$, Mo atoms are octahedrally coordinated and form a 3D structure of corner-sharing MoO_6 octahedra. The Ba atoms are found between the chains in 12-fold cuboctahedral coordination. The continuous 3D lattice of strong Mo−O bonds ensures the structure's rigidity and constrains the expansion of the weaker Ba−O bonds. The quaternary $Ba_2NaMoO_{5.5}$ shows the same 3D arrangement, except that half of the MoO_6 octahedra are replaced by NaO_6 octahedra. The Mo^{VI}−O bonds, alternating with much weaker Na^{I}−O bonds, result in a much stronger thermal expansion. The Ba−O bond length in $Ba_2NaMoO_{5.5}$ is also higher than in $BaMoO_3$, as observed by neutron diffraction (2.940(1) Å in this work vs 2.857 Å, as reported by Nassif et al.[33]), which indicates weaker Ba−O bonds in the quaternary compound. This property, together with the less-restraining octahedral network, explains a significantly higher swelling. Therefore, an increased swelling of the irradiated fuel is to be expected, in the case of the formation of this quaternary phase, following the interaction with the sodium coolant.

3.4. High-Temperature Raman Spectroscopy. Five sets of bands associated with the internal modes of vibration of the MoO_6 units are observed in the $Ba_2NaMoO_{5.5}$ Raman spectrum at room temperature (Figure 7), which are consistent with the data reported for $MeMoO_4$ (Me = Ba, Ca, Pb, Sr)[34−36] and for $Cs_3Na(MoO_4)_2$.[37]

Liegeois-Duyckaerts and Tarte[34] studied $A_2B^{II}B^{VI}O_6$ (A = Ba, Pb, Sr; B = Ba, Sr, Ca, Cd, Zn, Cu, Co, Ni, Mg) ordered perovskites with Raman spectroscopy. In the different spectra obtained, they attributed the highest-frequency band with a strong intensity ($\nu_1 \approx 891$ cm^{-1}) to the totally symmetric stretching of the MoO_6 octahedron in the internal modes approximation. The vibrations between 780 cm^{-1} and 850 cm^{-1} (ν_3) are associated with the antisymmetric stretching of the MoO_6 octahedron. In this range of frequencies, a wide feature is also observed due to the defects of the octahedron, which partly break the symmetry.[38] This is consistent with the neutron diffraction and EXAFS results (oxygen vacancies and tilting of the angles of the Mo−O−Mo−O bond). The peaks obtained at ∼300 and 380 cm^{-1} are associated with the antisymmetric (ν_4) and the symmetric (ν_2) bending modes. The external modes at low frequencies (50 to 110 cm^{-1}) are associated with the translation of the Na^+ cation.[34,39,40]

No noticeable change in the spectrum is seen between room temperature and 993 K, as observed in Figure 8, except for a

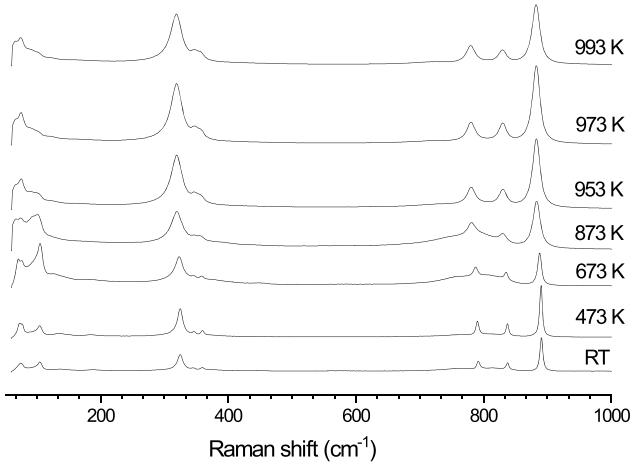

Figure 8. Variation of the Raman spectrum of $Ba_2NaMoO_{5.5}$ versus temperature.

slight widening of the peaks and shift in the wavenumber due to anharmonic effects appearing with increasing temperature.[41] Moreover, the bands position shift with temperature follows a linear function, as reported in Table 5, as well as Figure S5 in the Supporting Information. These results are consistent with the HT-XRD data, which also do not reveal any phase transition nor melting up to 1223 K. Moreover, a DSC measurement performed in this work up to 1473 K also did not show any phase transition nor melting of the compound. Hence, the quaternary $Ba_2NaMoO_{5.5}$ compound is determined to be stable up to at least 1473 K.

https://dx.doi.org/10.1021/acs.inorgchem.0c00210
Inorg. Chem. 2020, 59, 6120−6130

Table 5. Linear Thermal Shift Rate of the Different Band Positions in the $Ba_2NaMoO_{5.5}$ Compound

frequency	linear thermal shift rate (K^{-1} cm^{-1})
ν_1	−0.0134
ν_3-High	−0.0131
ν_3-Low	−0.0186
ν_2	−0.01

3.5. Solution Calorimetry Measurement of the Standard Enthalpy of Formation. The standard enthalpy of formation of $Ba_2NaMoO_{5.5}$ at 298.15 K was obtained in 2 M HNO_3 solution (VWR Chemicals, 99.5%) using the thermodynamic cycle detailed in Table 6. The dissolutions of $Ba_2NaMoO_{5.5}$, BaO, and $Na_2Mo_2O_7$ in nitric acid were, in all cases, instantaneous and complete. The calorimetric results of the three compounds dissolution are reported in Table 6.

To ensure that sol. 1 and sol 3 had the same final composition, a specific amount of sample was dissolved into solution. The detail of the calorimetric measurements is reported in Table 7. The enthalpy of formation from the constituting oxides BaO and $Na_2Mo_2O_7$ is equal to

$$\Delta_r H^\circ_m = \Delta_r H^\circ_{2a} + \Delta_r H^\circ_{2b} - \Delta_r H^\circ_1 = -306.24 \pm 0.65 \text{ kJ mol}^{-1}$$

corresponding to the following reaction:

$$\frac{1}{2}Na_2Mo_2O_{7(cr)} + 2BaO_{(cr)} = Ba_2NaMoO_{5.5(cr)}$$

The enthalpy of dissolution of BaO in a 1 M HCl solution has been measured in the work of Fitzgibbon et al.[42] They reported $\Delta_r H^\circ_m$ (298.15 K) = −(273.17 ± 0.96) kJ mol^{-1}, which is relatively close to the present data measured in a solution of 2 M HNO_3, i.e., −(284.19 ± 0.17) kJ mol^{-1}. To the best of our knowledge, there have not been measurements of the dissolution of $Na_2Mo_2O_7$ in acidic solution reported in the literature.

Combining with the standard enthalpy of formation of $BaO_{(cr)}$,[42] and $Na_2Mo_2O_{7(cr)}$,[43] the standard enthalpy of formation of $Ba_2NaMoO_{5.5}$ is finally derived as $\Delta_f H^\circ_m$ = −(2524.75 ± 4.15) kJ mol^{-1}.

3.6. Margin to the Safe Operation of SFRs. In a severe accident scenario, the $BaMoO_3$ (dissolved in the gray phase), $BaMoO_4$, and BaO phases formed during irradiation[6] could interact with the liquid sodium at different stages of a severe accident and form the $Ba_2NaMoO_{5.5}$ compound. Several equilibrium reactions could be envisaged:

$$BaMoO_4 + BaO + Na_{(l)} + \frac{1}{4}O_2 \rightarrow Ba_2NaMoO_{5.5} \quad (1a)$$

$$BaMoO_3 + BaO + Na_{(l)} + \frac{3}{4}O_2 \rightarrow Ba_2NaMoO_{5.5} \quad (2)$$

$$2BaO + Na_{(l)} + MoO_3 + \frac{1}{4}O_2 \rightarrow Ba_2NaMoO_{5.5} \quad (3)$$

$$2BaO + Na_{(l)} + MoO_2 + \frac{3}{4}O_2 \rightarrow Ba_2NaMoO_{5.5} \quad (4)$$

$$2BaO + Na_{(l)} + Mo_{(cr)} + \frac{7}{4}O_2 \rightarrow Ba_2NaMoO_{5.5} \quad (5)$$

Considering that the sodium is quasi-pure, with very little oxygen dissolved (typically 3 wppm under normal operation conditions),[44] the partial Gibbs energy of sodium $\Delta\overline{G_{Na}}$ was considered to be zero. Therefore, the equilibrium oxygen potential for the different reactions can be expressed as

$$\Delta\overline{G^{eq}_{O_2}}(T) = RT\ln\left(\frac{P_{O_2}}{P^\circ}\right) = 4[\Delta_f G^\circ_m(Ba_2NaMoO_{5.5}, s, T) - \Delta_f G^\circ_m(BaMoO_4, s, T) - \Delta_f G^\circ_m(BaO, s, T)] \quad (1')$$

$$\Delta\overline{G^{eq}_{O_2}}(T) = RT\ln\left(\frac{P_{O_2}}{P^\circ}\right) = \frac{4}{3}[\Delta_f G^\circ_m(Ba_2NaMoO_{5.5}, s, T) - \Delta_f G^\circ_m(BaMoO_3, s, T) - \Delta_f G^\circ_m(BaO, s, T)] \quad (2')$$

$$\Delta\overline{G^{eq}_{O_2}}(T) = RT\ln\left(\frac{P_{O_2}}{P^\circ}\right) = 4[\Delta_f G^\circ_m(Ba_2NaMoO_{5.5}, s, T) - \Delta_f G^\circ_m(MoO_3, s, T) - 2\Delta_f G^\circ_m(BaO, s, T)] \quad (3')$$

$$\Delta\overline{G^{eq}_{O_2}}(T) = RT\ln\left(\frac{P_{O_2}}{P^\circ}\right) = \frac{4}{3}[\Delta_f G^\circ_m(Ba_2NaMoO_{5.5}, s, T) - \Delta_f G^\circ_m(MoO_2, s, T) - 2\Delta_f G^\circ_m(BaO, s, T)] \quad (4')$$

Table 6. Reaction Cycle[a]

cycle	reaction	$\Delta_r H^\circ_m$ (298.15 K) (kJ mol^{-1})	uncertainty[b]	reference
(1)	$Ba_2NaMoO_{5.5}(s) + xHNO_3$ = sol. 1	−276.68	0.55	this work
(2a)	$2BaO(s) + xHNO_3$ = sol. 2	−568.38	0.34	this work
(2b)	$(1/2)Na_2Mo_2O_7(s)$ + sol. 2 = sol. 3	−14.55	0.09	this work
(3)	$Ba(s) + (1/2)O_2(g) = BaO(s)$	−548.00	2.00	42
(4)	$2Na(s) + 2Mo(s) + (7/2)\ O_2(g) = Na_2Mo_2O_7(s)$	−2245.02	1.81	43
(5)	$\mathbf{2Ba(s) + Na(s) + Mo(s) + (11/4)O_2(g) = Ba_2NaMoO_{5.5}(s)}$	**−2524.75**	**4.15**	this work

[a]Measurements were done at a pressure of p = 0.105 ± 0.005 MPa, and in the temperature interval of T = 298.15 ± 0.30 K. [b]Uncertainties correspond to the standard ones.

https://dx.doi.org/10.1021/acs.inorgchem.0c00210
Inorg. Chem. 2020, 59, 6120−6130

Table 7. Calorimetric Data for the Dissolution of $Ba_2NaMoO_{5.5}$ (M = 481.6 g mol^{-1}), BaO (M = 153.3 g mol^{-1}), and $Na_2Mo_2O_7$ (M = 349.9 g mol^{-1}) in 2 mol L^{-1} HNO_3 at 298.15 K (Uncertainties u on Molar Concentrations are $u(C)$ = 0.002 mol L^{-1})[a]

No.	mass of the sample, m[b] (mg)	temperature change, ΔT[c] (mK)	energy equivalent of the calorimeter, Cp[d] (J K^{-1})	Q[e] (J)	molar enthalpy of reaction, $\Delta_r H^\circ_m$(298.15 K)[f] (kJ mol^{-1})
			$Ba_2NaMoO_{5.5}$		
1	44.0	61.445	411.728	−25.298	−276.90
2	44.0	61.306	411.102	−25.203	−275.86
3	44.0	61.477	411.592	−25.303	−276.96
4	44.0	61.639	410.585	−25.308	−277.01
5	43.9	60.740	411.520	−24.996	−274.22
			BaO		
1	28.0	411.156	126.268	−51.916	−284.29
2	28.0	411.353	126.234	−51.927	−284.35
3	28.0	411.654	125.998	−51.868	−284.03
4	28.0	411.365	126.066	−51.859	−283.98
5	28.0	411.152	126.273	−51.917	−284.30
			$Na_2Mo_2O_7$		
1	16.0	409.511	3.257	−1.334	−29.17
2	15.9	411.617	3.157	−1.299	−28.40
3	16.0	411.108	3.226	−1.326	−28.99
4	16.0	409.800	3.263	−1.337	−29.24
5	15.9	410.749	3.189	−1.31	−28.82

[a]Solution calorimetry measurements were performed at a pressure of p = 0.105 ± 0.005 MPa, and in the temperature interval of T = 298.15 ± 0.30 K. (For pressure and temperature, the reported uncertainty is the standard uncertainty.) [b]Uncertainties u on the weights are u(m) = 0.1 mg. [c]Temperature change associated with the dissolution. The reported uncertainty on ΔT is $u_r(\Delta T)$ = 0.2. [d]The reported uncertainty on Cp is u_r(Cp) = 0.2. [e]Amount of heat generated by the dissolution. The reported uncertainty on Q is $u_r(Q)$ = 0.3. [f]The reported uncertainty on $\Delta_r H^\circ_m$(298.15 K) are $u_r(\Delta_r H^\circ_m(298.15\ K))$ = 0.4.

$$\Delta\overline{G^{eq}_{O_2}}(T) = RT\ln\left(\frac{P_{O_2}}{P^\circ}\right) = \frac{4}{7}[\Delta_f G^\circ_m(Ba_2NaMoO_{5.5}, s, T) - 2\Delta_f G^\circ_m(BaO, s, T)] \quad (5')$$

with P° the standard pressure (equal to 1 bar), P_{O_2} the oxygen partial pressure, $\Delta_f G^\circ_m$ the Gibbs energy of formation of $Ba_2NaMoO_{5.5}$, $BaMoO_4$, $BaMoO_3$, BaO, MoO_3, MoO_2, respectively. T is the temperature and R the universal gas constant.

The expected temperature of the sodium coolant is ∼680 K when entering the reactor core, and 823 K[45] as an average above the core, and will increase during an accident. Therefore, the possible formation of $Ba_2NaMoO_{5.5}$ was studied in this work up to the maximum temperature to which it is known to be stable (1473 K).

Using the thermodynamic functions listed in Tables S3 and S4 in the Supporting Information for the different compounds reported in eqs 1, 2, 3, 4, and 5), the threshold oxygen potential of formation of $Ba_2NaMoO_{5.5}$ was derived for the different reactions. They are listed in Table 8. The standard entropy at 298.15 K of the quaternary phase, and its heat capacity at high temperature are still unknown and were estimated in this work with a simple additive rule (entropy) and the Neumann−Kopp rule (heat capacity) applied to Na_2MoO_4,[40] BaO,[46] and MoO_3.[47]

With a procedure similar to that of Smith et al.,[40] the threshold derived for each reaction was subsequently compared to the concentration levels of oxygen dissolved in liquid sodium. Combining the oxygen solubility equation in sodium reported by Noden[4849] with the Gibbs energy of formation of Na_2O, the oxygen potential limit in sodium is given by[50]

$$\Delta\bar{G}^{eq}_0(T/K) = -735691.3 + (33.232 + 38.287\log C_0)T\ \text{J mol}^{-1}$$

where C_0 is the dissolved concentration in liquid sodium.

Table 8. Threshold for the Onset of Formation of $Ba_2NaMoO_{5.5}$

equilibrium	$\Delta\overline{G^{eq}_{O_2}}(T) = A + BT$ (kJ mol^{-1}) A	B	C_o(900 K) (wppm)	C_o(1400 K) (wppm)
1	−1724.566	0.28284	$<10^{-17}$	$\sim10^{-12}$
2	−989.339	0.19840	$\sim10^{-3}$	0.1−1
3	−2747.016	0.27884	$<10^{-17}$	−
4	−1118.326	0.17801	10^{-7}−10^{-8}	10^{-4}−10^{-5}
5	−813.954	0.17805	10−100	100−1000

Figure 9 shows the oxygen potential thresholds of formation of $Ba_2NaMoO_{5.5}$, considering all of the reactions (reactions 1−5). Under normal operation, the oxygen level in sodium is expected to be ∼3 wppm.[44] Therefore, at the beginning of the accident, all of the reactions would be possible, except for reaction 5 with metallic molybdenum. However, during an accident, the oxygen potential can increase, and therefore the reaction with metallic molybdenum (reaction 5) could be expected. Note that the oxygen potential threshold for the other four mechanisms is lower than that for the formation of the trisodium uranate (Na_3UO_4), which is the phase predicted to form in case of interaction between sodium and hyper-stoichiometric uranium dioxide.[50]

The most favorable reaction is that with BaO and MoO_3, which form at high burnup. Nevertheless, the barium molybdate compounds $BaMoO_3$ and $BaMoO_4$ could also

https://dx.doi.org/10.1021/acs.inorgchem.0c00210
Inorg. Chem. 2020, 59, 6120−6130

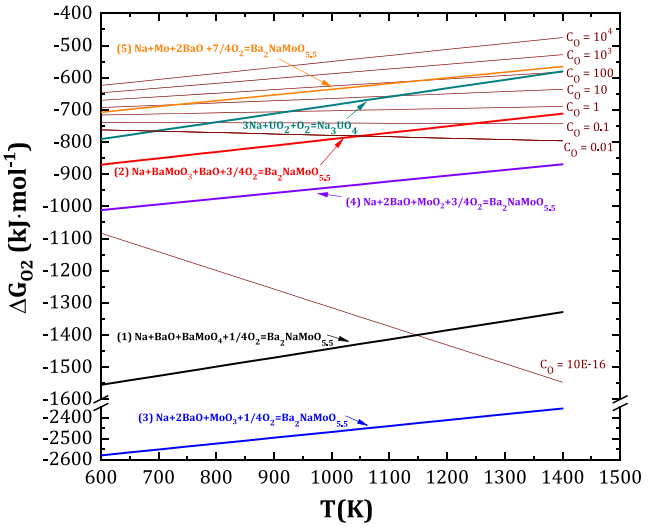

Figure 9. Threshold oxygen potential for the formation of $Ba_2NaMoO_{5.5}$ considering the reactions that could occur under accident conditions in a SFR and comparison with sodium uranate Na_3UO_4[50] and the oxygen levels in liquid sodium (C_0 in wppm), considering the solubility equation of Noden[48,49].

react both with BaO and liquid sodium to form $Ba_2NaMoO_{5.5}$. Therefore, from a thermodynamic point of view, the quaternary compound $Ba_2NaMoO_{5.5}$ could be formed under accidental conditions.

4. CONCLUSIONS

A detailed study of the crystal structure of the quaternary perovskite phase $Ba_2NaMoO_{5.5}$ is reported in this work by combining neutron diffraction, Raman spectroscopy, and EXAFS data. The hexavalent molybdenum valence state has also been confirmed from XANES spectroscopy measurements at the Mo K-edge. HT-XRD measurements performed in the temperature range of 303−1223 K have allowed us to derive the volumetric thermal expansion coefficient as $\alpha_{vol} = 55.8 \times 10^{-6}$ K^{-1}, which is ∼2 times higher than that of the ternary barium molybdate compounds $BaMoO_3$ and $BaMoO_4$ formed in the irradiated fuel under certain conditions. The high thermal expansion was explained in relation with the local structural arrangement. No phase transition was observed, neither in the HT-XRD, Raman spectroscopy, nor DSC measurements, showing that this quaternary perovskite phase is stable up to at least 1473 K. Moreover, the enthalpy of formation was derived from solution calorimetry measurements as $\Delta_f H^\circ_m(Ba_2NaMoO_{5.5}, cr, 298.15\ K) = -(2524.75 \pm 4.15)$ kJ mol^{-1}. The oxygen potential thresholds for the formation of the quaternary compound were finally derived considering different reaction mechanisms between liquid sodium and fission products phases in irradiated $U_{1-x}Pu_xO_2$ fuel. It was found that, in cases where barium oxide would be present together with MoO_2, MoO_3, $BaMoO_3$ or $BaMoO_4$, the contact with liquid sodium would lead to the formation of $Ba_2NaMoO_{5.5}$; hence, the thermodynamic and thermophysical properties of this phase are important for the SFR safety analysis. However, $BaMoO_3$ is not found as a pure compound in the irradiated fuel but in solution in the gray phase $(Ba,Cs,Sr)(Zr,U,Pu,Mo,RE)O_3$ (RE = rare earths). Therefore, it would be highly interesting and relevant to extend this study to the entire phases formed in the "gray phase", with the end goal to develop a full thermodynamic assessment of the Na-Ba-Cs-Na-Mo-Sr-Zr-U-Pu-RE-O system using the CALPHAD method. The present results will be used as input for the assessment of the Ba-Mo-Na-O system, as part of a wider research program in our group dedicated to the development of a Na-U-Pu-O-FPs database (where FPs = fission products).

■ ASSOCIATED CONTENT

Supporting Information

The Supporting Information is available free of charge at https://pubs.acs.org/doi/10.1021/acs.inorgchem.0c00210.

XRD and neutron diffraction crystallographic files in CIF format of $Ba_2NaMoO_{5.5}$; XRD patterns of the $BaMoO_4$ and $Na_2Mo_2O_7$; DSC heat flow curve of the $Na_2Mo_2O_7$; neutron diffraction pattern at λ = 1.33 Å and atomic positions after refinement of $Ba_2NaMoO_{5.5}$; lattice parameters evolution of $Ba_2NaMoO_{5.5}$, as a function of the temperature; evolution of the Raman band position of $Ba_2NaMoO_{5.5}$, as a function of the temperature; thermodynamic data used in the thermodynamic equilibrium calculations. (PDF)

■ AUTHOR INFORMATION

Corresponding Authors

Anna L. Smith − *Faculty of Applied Sciences, Radiation Science & Technology Department, Delft University of Technology, 2629 Delft, The Netherlands*; orcid.org/0000-0002-0355-5859; Email: a.l.smith@tudelft.nl

Christine Guéneau − *DEN-Service de la Corrosion et du Comportement des Matériaux dans leur Environnement (SCCME), CEA, Université Paris-Saclay, F-91191 Gif-sur Yvette, France*; Email: christine.gueneau@cea.fr

Authors

Guilhem Kauric − *DEN-Service de la Corrosion et du Comportement des Matériaux dans leur Environnement (SCCME), CEA, Université Paris-Saclay, F-91191 Gif-sur Yvette, France*

Enrica Epifano − *Faculty of Applied Sciences, Radiation Science & Technology Department, Delft University of Technology, 2629 Delft, The Netherlands*

Philippe M. Martin − *CEADEN, DMRC, Univ. Montpellier, Marcoule, France*

Lambert van Eijck − *Faculty of Applied Sciences, Radiation Science & Technology Department, Delft University of Technology, 2629 Delft, The Netherlands*

Daniel Bouëxière − *European Commission, Joint Research Center, D-76125 Karlsruhe, Germany*

Nicolas Clavier − *CEA, CNRS, ENSCM, ICMS, Univ Montpellier, Bagnols-sur-Cèze, France*

Complete contact information is available at: https://pubs.acs.org/10.1021/acs.inorgchem.0c00210

Notes

The authors declare no competing financial interest.

■ ACKNOWLEDGMENTS

The authors would like to thank J. Vlieland for the KCl calibration measurements of the solution calorimeter at TU Delft. The authors are also thankful to the support team of the BM26A beamline and, in particular, to Banerjee Dipanjan for the help received during the XAS experiments.

■ ADDITIONAL NOTE

[#]Four *lcc* path* details: Mo(c) → O(1) (180°) → Mo(c) 0° → O(2) 180°→ Mo(c)).

■ REFERENCES

(1) Kelly, J. E. Generation IV International Forum: A decade of progress through international cooperation. *Prog. Nucl. Energy* **2014**, *77*, 240−246.

(2) Imoto, S. Chemical state of fission products in irradiated UO_2. *J. Nucl. Mater.* **1986**, *140*, 19−27.

(3) Paschol, J. O. A.; Kleykamp, H.; Thümmler, F. Phase equilibria in the pseudoquaternary BaO-UO_2-ZrO_2-MoO_2 system. *J. Nucl. Mater.* **1987**, *151*, 10−21.

(4) Muromura, T.; et al. Metallic phases precipitated in UO_2 fuel: I. Phases in simulated fuel. *J. Nucl. Mater.* **1988**, *151*, 327−333.

(5) Kurosaki, K.; Tanaka, K.; Osaka, M.; Ohishi, Y.; Muta, H.; Uno, M.; Yamanaka, S. Chemical States of Fission Products and Actinides in Irradiated Oxide Fuels Analyzed by Thermodynamic Calculation and Post-Irradiation Examination. *Prog. Nucl. Sci. Technol.* **2011**, *2*, 5−8.

(6) Kleykamp, H. The chemical state of the fission products in oxide fuels. *J. Nucl. Mater.* **1985**, *131*, 221−246.

(7) Barrachin, M.; Gavillet, D.; Dubourg, R.; De Bremaecker, A. Fuel and fission product behaviour in early phases of a severe accident. Part I: Experimental results of the PHEBUS FPT2 test. *J. Nucl. Mater.* **2014**, *453*, 340−354.

(8) IRSN. *La gestion des accidents graves*. Available via the Internet at: http://www.irsn.fr/FR/connaissances/Installations_nucleaires/Les-centrales-nucleaires/accidents-graves/Pages/sommaire.aspx#.WythBqczbb0, 2018.

(9) NEA Nuclear Science Committee. *Thermodynamics of Advanced Fuels − International Database (TAF-ID)*. 2017. https://www.oecd-nea.org/science/taf-id/.

(10) Geiger, E.; Guéneau, C.; Pontillon, Y.; Corcoran, E. C. Modelling nuclear fuel behaviour with TAF-ID: Calculations on the VERDON-1 experiment, representative of a nuclear severe accident. *J. Nucl. Mater.* **2019**, *522*, 294−310.

(11) Samuelsson, K.; Dumas, J.-C.; Sundman, B.; Lamontagne, J.; Guéneau, C. Simulation of the chemical state of high burnup (U, Pu) O 2 fuel in fast reactors based on thermodynamic calculations. *J. Nucl. Mater.* **2020**, *532*, 151969.

(12) Lukas, H. L.; Fries, S. G.; Sundman, B. *Computational Thermodynamics: The Calphad Method*; Elsevier, 2007 (DOI: 10.1017/CBO9780511804137).

(13) Sabatier, R.; Wathlé, M.; Besse, J. P.; Baud, G. Perovskites oxyfluorées et oxygénées. *J. Inorg. Nucl. Chem.* **1971**, *33*, 1597−1613.

(14) Thangadurai, V.; Shukla, A. K.; Gopalakrishnan, J. Oxide-ion conduction in anion-deficient double perovskites, $Ba_2BB'O_{5.5}$ (B = Li, Na; B′=Mo, W, Te). *Solid State Ionics* **1997**, *104*, 277−283.

(15) van Eijck, L.; et al. Design and performance of a novel neutron powder diffractometer: PEARL at TU Delft. *J. Appl. Crystallogr.* **2016**, *49*, 1398−1401.

(16) Rodriguez-Carvajal, J. Recent advances in magnetic structure determination by neutron powder diffraction. *Phys. B* **1993**, *192*, 55−69.

(17) Taylor, D. Thermal expansion. Binary oxides with the silica structures. *Br. Ceram. Trans., J.* **1984**, *83*, 5−9.

(18) Nikitenko, S.; et al. Implementation of a combined SAXS/WAXS/QEXAFS set-up for time-resolved in situ experiments. *J. Synchrotron Radiat.* **2008**, *15*, 632−640.

(19) Ravel, B.; Newville, M. ATHENA, ARTEMIS, HEPHAESTUS: data analysis for X-ray absorption spectroscopy using IFEFFIT. *J. Synchrotron Radiat.* **2005**, *12*, 537−541.

(20) Rehr, J. J.; Albers, R. C. Theoretical approaches to x-ray absorption fine structure. *Rev. Mod. Phys.* **2000**, *72*, 621−654.

(21) Beneš, O.; Konings, R. J. M.; Wurzer, S.; Sierig, M.; Dockendorf, A. A DSC study of the $NaNO_3$−KNO_3 system using an innovative encapsulation technique. *Thermochim. Acta* **2010**, *509*, 62−66.

(22) Uriano, G. A. Potassium Chloride KCl(cr) for Solution Calorimetry; SRM 1655; National Bureau of Standards: Washington, D.C., 1981.

(23) Parker, V. B. Thermal Properties of Uni-univalent Electrolytes, *National Standard Reference Data Series*, Vol. *2*; National Bureau of Standards, 1965.

(24) Wadsö, I.; Goldberg, R. N. Standards in isothermal microcalorimetry (IUPAC Technical Report). *Pure Appl. Chem.* **2001**, *73*, 1625−1639.

(25) Wagman, D. D.; Evans, W. H.; Parker, V. B.; Schumm, R. H.; Halow, I.; Bailey, S. M.; Churney, K. L.; Nuttall, R. L. *J. Phys. Chem. Ref Data* **1971**, *11* and erratum (1989, https://doi.org/10.1063/1.555845).

(26) Loopstra, B. O. Neutron powder diffractometry using a wavelength of 2.6 Å. *Nucl. Instrum. Methods* **1966**, *44*, 181−187.

(27) Kumar, D.; Sathe, V. G. Raman spectroscopic study of structural transformation in ordered double perovskites La2CoMnO6 bulk and epitaxial film. *Solid State Commun.* **2015**, *224*, 10−14.

(28) Aritani, H.; et al. Structure of Mo−Mg Binary Oxides in Oxidized/Reduced States Studied by X-ray Absorption Spectroscopy at the Mo K Edge and Mg K Edge. *J. Phys. Chem.* **1996**, *100*, 5440−5446.

(29) Kuzmin, A.; Purans, J. Dehydration of the molybdenum trioxide hydrates $MoO_3.n\ H_2O$: *in situ* x-ray absorption spectroscopy study at the Mo K edge. *J. Phys.: Condens. Matter* **2000**, *12*, 1959−1970.

(30) Rocca, F.; Kuzmin, A.; Mustarelli, P.; Tomasi, C.; Magistris, A. XANES and EXAFS at Mo K-edge in $(AgI)_{1-x}(Ag_2MoO_4)_x$ glasses and crystals. *Solid State Ionics* **1999**, *121*, 189−192.

(31) Sahu, M.; et al. Characterization and thermo physical property investigations on $Ba_{1-x}Sr_xMoO_4$ (x = 0, 0.18, 0.38, 0.60, 0.81, 1) solid-solutions. *J. Nucl. Mater.* **2012**, *427*, 323−332.

(32) Sahu, M.; Krishnan, K.; Saxena, M. K.; Dash, S. Thermophysical properties of $Ba_{1-x}Sr_xMoO_{3\ (s)}$. *J. Nucl. Mater.* **2015**, *457*, 29−35.

(33) Nassif, V.; Carbonio, R. E.; Alonso, J. A. Neutron Diffraction Study of the Crystal Structure of BaMoO4: A Suitable Precursor for Metallic BaMoO3 Perovskite. *J. Solid State Chem.* **1999**, *146*, 266−270.

(34) Liegeois-Duyckaerts, M.; Tarte, P. Vibrational studies of molybdates, tungstates and related compounds—II: New Raman data and assignments for the scheelite-type compounds. *Spectrochim. Acta Part Mol. Spectrosc.* **1972**, *28*, 2037−2051.

(35) Basiev, T. T.; Sobol, A. A.; Voronko, Yu. K.; Zverev, P. G. Spontaneous Raman spectroscopy of tungstate and molybdate crystals for Raman lasers. *Opt. Mater.* **2000**, *15*, 205−216.

(36) Wallez, G.; Raison, P. E.; Smith, A. L.; Clavier, N.; Dacheux, N. High-temperature behavior of dicesium molybdate Cs_2MoO_4: Implications for fast neutron reactors. *J. Solid State Chem.* **2014**, *215*, 225−230.

(37) Smith, A. L.; et al. Structural and thermodynamic study of $Cs_3Na(MoO_4)_2$: Margin to the safe operation of sodium cooled fast reactors. *J. Solid State Chem.* **2019**, *269*, 1−8.

(38) Scheetz, B. E.; White, W. B. Characterization of Anion Disorder in Zirconate $A_2B_2O_7$ Compounds by Raman Spectroscopy. *J. Am. Ceram. Soc.* **1979**, *62*, 468−470.

(39) Saraiva, G. D.; et al. Temperature-dependent Raman scattering studies on $Na_2Mo_2O_7$ disodium dimolybdate. *J. Raman Spectrosc.* **2011**, *42*, 1114−1119.

(40) Smith, A. L.; et al. Structural and thermodynamic study of Cs3Na(MoO4)2: Margin to the safe operation of sodium cooled fast reactors. *J. Solid State Chem.* **2019**, *269*, 1−8.

(41) Kokanyan, N.; Chapron, D.; Fontana, M. D. Temperature dependence of Raman scattering and anharmonic properties in $LiNbO_3$. *Appl. Phys. A: Mater. Sci. Process.* **2014**, *117*, 1147−1152.

(42) Fitzgibbon, G. C.; Huber, E. J., JR.; Holley, C. E., JR. The enthalpy of formation of barium monoxide. *J. Chem. Thermodyn.* **1973**, *5*, 577−582.

https://dx.doi.org/10.1021/acs.inorgchem.0c00210
Inorg. Chem. 2020, 59, 6120−6130

(43) Tangri, R. P.; Venugopal, V.; Bose, D. K. Standard molar enthalpies of formation of sodium molybdates ($Na_2Mo_nO_{3n+1}$ with n = 1, 2, 3 or 4) at 298.15 K by solution calorimetry. *Thermochim. Acta* **1992**, *198*, 259−265.
(44) Kleykamp, H. *Assessment of the physico-chemical properties of phases in the Na-U-Pu-O system*, Technical Report No. KfK-4701, 1990; 31 pp.
(45) Guerin, Y. Fuel Performance of Fast Spectrum Oxide Fuel. In *Comprehensive Nuclear Materials*; Elsevier, 2012; Chapter 2.21, pp 547−578.
(46) Cordfunke, E. H. P.; van der Laan, R. R.; van Miltenburg, J. C. Thermophysical and thermochemical properties of BaO and SrO from 5 to 1000 K. *J. Phys. Chem. Solids* **1994**, *55*, 77−84.
(47) Cordfunke, E. H. P.; Konings, R. J. M. *Thermochemical Data for Reactor Materials and Fission Products*; Elsevier Science Publishers B.V., 1990.
(48) Noden, J. D. General equation for the solubility of oxygen in liquid sodium. *J. Br. Nucl. Energy Soc.* **1973**, *12*, 57−62.
(49) Noden, J. D. General equation for the solubility of oxygen in liquid sodium. Addendum. *J. Br. Nucl. Energy Soc.* **1973**, *12*, 329−331.
(50) Smith, A. L.; et al. Thermodynamic assessment of the Na-O and Na-U-O systems: Margin to the safe operation of SFRs. *J. Chem. Thermodyn.* **2017**, *114*, 93−115.

https://dx.doi.org/10.1021/acs.inorgchem.0c00210
Inorg. Chem. 2020, 59, 6120−6130